PROCEEDINGS, 46th Workshop on Geothermal Reservoir Engineering
Stanford University, Stanford, California, February 15-17, 2021
SGP-TR-218

Using Surface Deformation and Machine Learning to Determine State of Stress Changes at the Coso Geothermal Field, California USA

Sarah Roberts[1], Andrew Delorey[1], Christopher W. Johnson[1], Robert Guyer[1], Richard Alfaro-Diaz[1], Paul Johnson[1]

[1]Los Alamos National Laboratory, P.O. Box 663, Bikini Atoll Road, SM-30, Los Alamos, NM 87545

sarahr@lanl.gov; andrew.delorey@lanl.gov; cwj@lanl.gov; guyer@physics.umass.edu; raalfarodiaz@lanl.gov; paj@lanl.gov

Keywords: stress tensor, transient stress, machine learning, surface deformation

ABSTRACT

Tracking the state of stress evolution within geothermal reservoirs is important for optimizing energy production and characterizing seismic hazard. Borehole image analysis and hydraulic fracture tests can constrain principal stress directions and magnitudes at discrete locations, but cannot provide a full description of the evolving stress tensor throughout the reservoir. Interferometric synthetic aperture radar (InSAR) observations can reveal high-resolution, reservoir-scale, time-dependent surface displacements that can be used in inversion models to infer subsurface stress sources and changes in the stress tensor. However, such stress inversions are subject to various a priori assumptions, including source type, location, number, or magnitude.

We develop a novel method to obtain a description of the evolving stress field that utilizes machine learning (ML) to quantify subsurface stress tensor changes from InSAR observations. We train a convolutional neural network (CNN) with data produced using analytical realizations of subsurface strain and surface displacement from sources representing volumetric and double couple deformation. From the strain values we calculate subsurface stress in the geothermal reservoir. We establish the range of earthquake parameters and fluid pressure sources that produce InSAR-measurable surface displacements and train the CNN to characterize the stress field from surface displacements. In parallel with our CNN solution to the relationship between ground deformation and interior stress, we develop an independent solution employing a variational procedure. These two problem solutions are used interactively to inform the development of each. We demonstrate the application of our ML-based solution for the Coso Geothermal field. The success of our ML-based approach suggests that with generalized training, our method could be employed broadly to geothermal fields to provide field operators with a near real-time model of stress field evolution.

1. INTRODUCTION

The state of stress in a geothermal reservoir is constantly evolving in response to anthropogenic injection and production activities (Martínez-Garzón et al., 2013; Feng and Lees, 1998; Cardiff et al., 2018) and natural processes, which vary from site to site. Both anthropogenic pumping, and natural and induced earthquakes produce deformation of the injection field. A common practice to determine the sources of temporal stress change is to invert the surface displacements for analytical source dimensions, locations, and accompanying reservoir volume change, while considering elastic, poroelastic, and thermoelastic effects (Ali et al., 2016; Eneva et al., 2018; Fialko and Simons, 2000; Reinisch et al., 2020; Wicks et al., 2001). Reservoir stress at specific points in time can be estimated through forward modeling of the sources determined from the inversion. Another approach is to directly invert earthquake focal mechanisms for principal stress orientations and relative magnitudes that vary with depth, geographic location, or time (e.g. Martínez-Garzón et al., 2013; Schoenball et al., 2014). Local reservoir stress magnitudes and orientations can also be estimated in boreholes via hydraulic fracturing stress tests (Sheridan and Hickman, 2004) or borehole image data analysis (Schoenball and Davatzes, 2017; Sheridan et al., 2003; Davatzes and Hickman, 2006; Blankenship et al., 2016).

Due to the evolving nature of reservoir stress, it is desirable to have a method for obtaining frequent, temporal updates to a stress model. All of the above approaches rely on methods or observations that cannot be regularly updated. While InSAR surface displacements are routinely or repeatedly collected in time, typical application of inversion approaches require manual setup of inversion routines using a known velocity structure. Updating a reservoir stress model through focal mechanism inversion involves waiting for a sufficient number of earthquakes suitable for focal mechanism estimation to occur in the region of interest (Hardebeck and Michael, 2006). Borehole methods provide stress only at discrete reservoir locations, and are costly and time-intensive to repeat.

Applying ML in earth science is an attractive alternative to traditional numerical modeling or inverse problems due to the enormous function space the models can explore (Bergen et al., 2019). In the case of stress modeling, few assumptions regarding deformation sources and velocity structure are required. Supervised learning approaches have been successfully utilized for many applications (Bergen et al., 2019; Ren et al., 2020); for instance, in place of classical full-waveform inversion (Wu and Lin, 2019), tomography (Araya-Polo et al., 2018), simulation of seismic wave propagation (Moseley et al., 2018), and volcanic ash particle classification (Shoji et al., 2018). Supervised ML techniques involve model training using a large set of labeled data. If trained on a sufficiently general set of training data, the ML model may be transferable to other locations without further training. In this paper we outline and demonstrate a supervised learning-based approach to determine temporal changes to the stress field in the Coso Geothermal field directly from surface displacements.

2. COSO GEOTHERMAL FIELD

The Coso Geothermal field (CGF; Figure 1) has been in operation since 1987 (Monastero, 2002). The field currently operates over 120 extraction and injection wells (Geothermal Well Search, 2020) and is among the top three producing geothermal sites in the U.S. Peak energy production of the field has been as high as 270 MW and presently nets about 145 MW (Coso Operating Company, 2020).

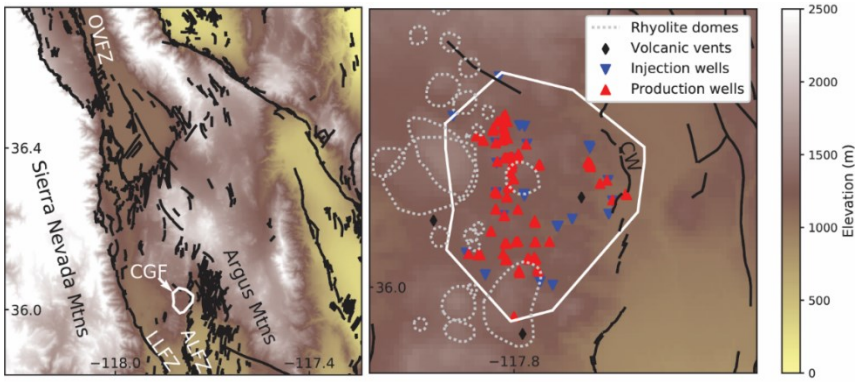

Figure 1: Regional (left) and local (right) maps of the Coso Geothermal field (CGF) area showing Quaternary faults (Jennings and Bryant, 2010) in black and topography (NASA Shuttle Radar Topography Mission Global 1 Arc Second, 2013). Faults delineating the Coso stepover are labeled on the left: Owens Valley Fault Zone (OVFZ), Little Lake Fault Zone (LLFZ), and Airport Lake Fault Zone (ALFZ). The Coso Wash (CW) fault delineating the eastern edge of the CGF is labeled on the right. White polygon borders the production field, with active production (red) and injection (blue) wells indicated by triangles. Pleistocene rhyolite domes (dotted lines) and basaltic vents (diamonds) (Bacon et al., 1981) dotting the field are shown on the right.

Satellite observations of CGF surface displacements going back to 1992 show field-centered subsidence at rates ranging from centimeters to millimeters per year (e.g. Fialko and Simons, 2000; Wicks et al., 2001; Reinisch et al., 2020). Monthly geothermal fluid extraction and injection data indicate extraction mass generally exceeds injection (Geothermal Production and Injection Data Maps, 2020). Early estimates of natural groundwater recharge (Figure 2) indicate excess extraction mass may be only partially compensated by groundwater flow from precipitation in the surrounding mountains (Spane, 1978). Many workers have interpreted field subsidence in terms of reservoir deflation. Fialko and Simons (2000) invert InSAR surface displacements from 1993-1999 for prolate spheroidal pressure sources. They find a maximum subsidence rate of 3-4 cm/yr, which they explain by 4 under-pressure and 1 minor over-pressure sources located between 1 and 3 km depth, due to either reservoir depletion or cooling. Wicks et al. (2001) invert the long-wavelength component of InSAR displacement from 1992-1997 for a slightly deeper deflationary source, which they interpret as depressurizing magmatic fluids entering the field from a deeper magma body. Ali et al. (2016) model InSAR deformation from 2004-2011 in terms of an under-pressurized oblate spheroid, which they argue is equally well explained by either declining pressure or thermoelastic contraction. Eneva et al. (2018) use poroelastic modeling of InSAR deformation from 2004-2010 and 2014-2018 to interpret reservoir depletion. They find a decreasing rate of subsidence between the two time periods analyzed, with the latest 2014-2018 maximum subsidence rate at 19.1 mm/yr as compared to 27.6 mm/yr for the 2004-2010 period (Eneva et al., 2018). From InSAR displacements, Reinisch et al. (2020) find a decreasing subsidence rate between 2004-2010 and 2014-2016 and explain the reduced subsidence rates in the later time period through a depletion-induced increase in reservoir depth. Whatever the source of deformation, the previous work consistently shows field-centered subsidence at a decreasing rate with time.

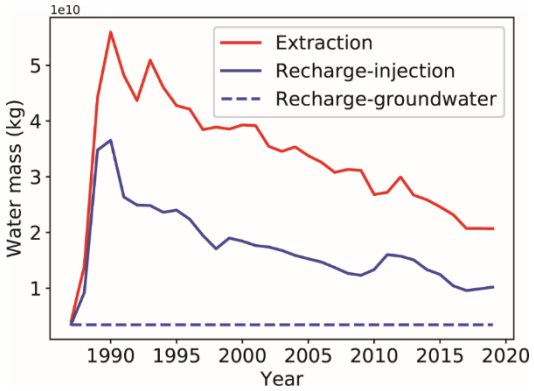

Figure 2: Mass of monthly geothermal fluid extraction and injection summed by year (solid lines) plotted with estimated annual groundwater recharge (dashed line) for the Coso Geothermal field.

Regional tectonic forces also contribute to field deformation. Located between the Sierra Nevada and Argus mountains in eastern California, the CGF is positioned in a releasing stepover between dextral strike-slip faults to the southwest (Little Lake and Airport Lake faults) and the northeast (Owens Valley fault) (Figure 1) (Monastero et al., 2005; Hauksson and Unruh, 2007). Regionally the field is in the southern Walker Lane belt, an active seismic zone of transtension governed by strike-slip displacement of the Sierran microplate to the northwest and extension in the southwest Basin and Range (Monastero et al., 2005; Hauksson and Unruh, 2007). Transtensional stress is manifested through two main types of faults located in the field: relatively dormant strike-slip faults trending WNW or NE, and currently active normal faults trending N to NNE (Sabin et al., 2015; Duffield et al., 1980; Davatzes and Hickman, 2006). Seismicity in the field tends to be low magnitude (M<2) and at shallow depths (<~5 km) (Figure 3) (Hauksson et al., 2012; Monastero et al., 2005; Hauksson and Unruh, 2007). The interconnected faults provide an important source of permeability in the CGF, and produce hydrothermal compartmentalization within the field (Sabin et al., 2015).

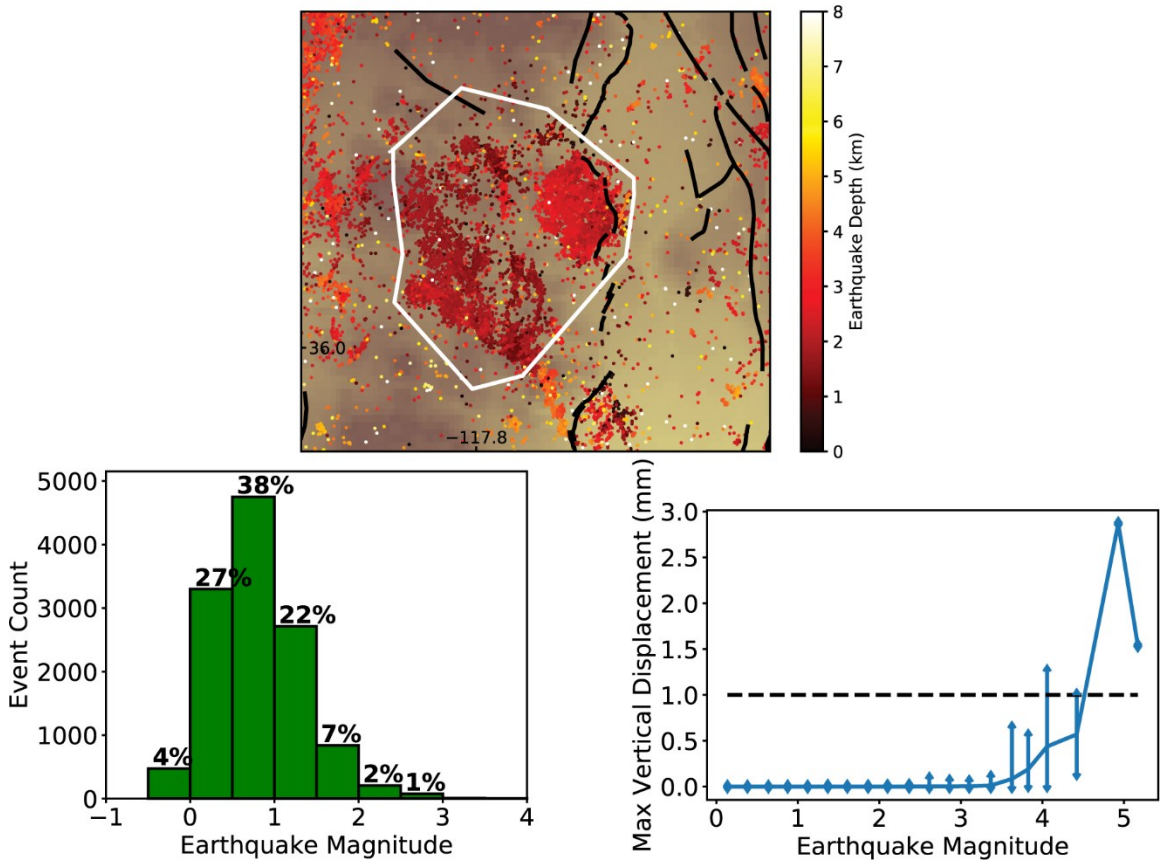

Figure 3: Earthquake hypocenter depths (Hauksson et al., 2012) are shallow (generally <5 km) in the CGF (bounded by white polygon in upper figure). Earthquake magnitudes within the CGF are generally in the microearthquake range (lower left). Lower right figure shows maximum vertical surface displacements (y-axis) inside the CGF, due to elastic dislocation models of earthquake focal mechanisms binned by magnitude (x-axis). Connected dots show average maximum vertical displacement inside the CGF over all earthquakes in bin. Error bars show minimum and maximum vertical displacement of all earthquakes in bin. We calculate surface displacements over all earthquakes with focal mechanism solutions occurring within 16 km of the center of the CGF. Only Mw 4+ events generally produce greater than 1 mm vertical surface displacements.

In addition to fault compartmentalization, lateral variations in reservoir gas and liquid compositions also divide the CGF into up to five compartments. Wells located in the southwest, central steam cap, and East Flank compartments are two-phase, containing approximately 5% - 29% steam fractions (Williams and Copp, 1991; Christenson et al., 2007; Buck, 2020). Wells located in the northwest and southeast are liquid-only (Williams and Copp, 1991). Ar-N_2 ratio variation between northern and southern wells indicate northern well fluids are precipitation-sourced while southern well fluids indicate a homogenous vapor source, potentially volcanic gas (Williams and Copp, 1991). Northern and southern wells are also delineated in depth and temperature. Northern wells produce fluids at temperatures less than 250°C and depths between 0.5 and 1 km, while southern wells produce fluids at greater than 300°C between 1.5 and 2 km depth (Feng and Lees, 1998). The deepest production well in the field operates at 3.8 km depth (Mhanna et al., 2018).

In alignment with hotter temperatures, analyses of production fluids indicate the thermal fluid source upwells in the southern part of the field and fans out to the north and east (Moore et al., 1989). Isotope signatures in Coso fluids and gases indicate the thermal fluid may have an asthenospheric source (Monastero et al., 2005). Geophysical evidence for the exact nature and location of the thermal source is variable. The field is characterized by rhyolitic domes and basaltic vents dated within the last 1 Ma (Bacon et al., 1981). Thermobarometric analysis of the erupted rhyolite indicates the magma source shallowed from 10 km to ~5.5 km depth between eruption episodes occurring 0.6 to ~0.3 Ma and 0.04 Ma (Manley and Bacon, 2000). Wicks et al. (2001) model the primary source of surface subsidence as a long, linear magmatic fluid source at ~4 km depth stretching NNE to SSW across the field, perpendicular to the direction of minimum compressive stress (Schoenball and Davatzes, 2017). Gravity data indicates a high density body at depth beneath the field, which has been interpreted as the combination of a dike complex and ultramafic asthenospheric diapir at depths greater than 6 km (Monastero et al., 2005), or as high density cold plutons underlain by low density partially molten rocks also at depths greater than 6 km (Wamalwa et al., 2013). Wamalwa et al. (2013) use an inverse model of magnetotelluric data to interpret a low resistivity zone below 6 km as a zone of partial melting. However, three-dimensional Vp/Vs models do not show a large body of pervasive melting beneath the field. Hauksson and Unruh (2007) and Zhang and Lin (2014) both find a lack of significantly high Vp/Vs zones, diagnostic of magma bodies, beneath the field. Hauksson and Unruh (2007) interpret a low velocity zone between 8 and 12 km depth as a region containing geothermal brines beneath the field with perhaps a 1 km^3 body at 10 km depth containing a small percent of melting. Similarly, Zhang and Lin (2014) interpret a low velocity zone between 6 and 12 km depth beneath the field as a frozen felsic body with water inclusions.

3. METHOD

3.1 Training data

The state of stress within the geothermal field is inferred using a CNN that is trained to translate InSAR surface displacements from volumetric and double couple source mechanisms. To obtain the large number of observations required for training a CNN, we rely on analytical simulations to produce the expected surface displacements from fluid injection and earthquakes. Simulations are calculated using half-space deformation models for shear and tensile fractures (Okada, 1992) that are constrained using documented injection volumes and historic earthquake activity.

The simulations consist of a randomly generated injection volume time series (305 time steps) that contain seasonal and interannual trends. At each time step, the volume is randomly distributed between 1-5 source locations that are randomly located in the model space between 0.5 – 3.0 km depth. The goal is to produce a very large number of scenarios ($>10^6$) that contain varying injection well locations, with different net injection, to capture the surface displacements from multiple sources. For each InSAR time series calculated, a conditional is tested if a random number drawn from a uniform distribution is >0.5, if true then earthquake deformation is included. The deformation from 1-5 earthquakes, randomly selected, with magnitudes ranging between $3.8<M<5.2$, are simulated at random locations from 1.5-6.0 km depth at a random time interval and propagated through the synthetic injection time series simulation. The magnitude and depth range of simulated earthquakes are chosen to capture events capable of producing InSAR-measurable surface displacement (on the order of 1 mm). The magnitude and depth ranges were determined by analytically modeling (Toda et al., 2011; Lin and Stein, 2004) surface displacements from focal mechanism solutions for cataloged earthquakes occurring in the Coso vicinity between 1981 and 2018 (Yang et al., 2012). The set range of events are capable of producing at least 1 mm vertical surface displacement within the CGF (Figure 3). The combined volumetric and double-couple sources at each time step are used to calculate the surface displacements (z=0 km) and the 6-component stress tensor on a two-dimensional grid at 4 depth intervals (z=1,2,3,4 km). Calculations are done assuming sources reside in a linear elastic formation with shear modulus of 30 GPa and Poisson ratio of 0.21, which are typical elastic properties for a homogeneous, igneous geothermal reservoir. We assume a continuously varying stress field and smooth the values within 1.5 km of each source to avoid numerical effects produced by the point source representation of the model. The procedure is repeated 4096 times to produce 1,249,280 synthetic examples of resolvable deformation in a geothermal reservoir.

3.2 Model design and training

The CNN model input is the two-dimension surface displacements (64x64x1) for a symmetric UNet architecture design consisting of 4 down-going layers, containing depths of 24, 48, 96, 192 and reducing the dimension with a 2x2 filter width, a stride of 2, a max pooling operator, and a ReLU activation function. The up-going layers are reversed with the corresponding symmetric layer concatenated to the two-dimension convolutional transpose, with the model depth decreasing to a final layer with a depth of 24 and a linear activation function, which represents an output shape of the two-dimensional grid and the 6 component stress tensor at 4 depth intervals (64x64x24). The synthetic examples are shuffled and 90% are used for training with 10% used in validation. The model is trained for 128 epochs using a batch size of 32 with the Adam version of the stochastic gradient descent to reduce the mean squared error of the stress tensor component estimates. A triangular decaying cyclic learning rate is applied with bounds between 10^{-4} to 10^{-2} for a 4 epoch cycle to reduce by a factor of 2-(n-1) each cycle, where n is the number of cycles completed. Early stopping is applied to avoid overfitting.

3.3 Application of InSAR to trained CNN model

The immediate goal is to apply the trained CNN to newly-acquired InSAR surface displacements and obtain updated stress tensor components at 4 depth intervals. InSAR deformation maps will be obtained through a novel, ML-based technique to produce denoised surface displacements with the ability to resolve millimeter-scale line-of-sight displacements (Rouet-Leduc et al., 2020). Currently, updated SAR observations of the CGF are available on a twelve-day repeat interval through the European Space Agency's Sentinel-1 constellation (Sentinel-1 Observation Scenario, 2021).

3.4 Benchmark trained CNN model

A key goal of this work is to determine whether our CNN approach predicts similar stress as traditional inversion-style approaches. We validate the CNN model results for InSAR-to-interior-stress problem by making comparison to the variational solution (Yourgrau and Mandelstam, 1979) of the InSAR-to-interior-strain problem. Comparison is made at the strain field level. The strain field is the primary output of the InSAR-to-interior-strain problem, while the strain field is a component of the InSAR-to-interior-stress problem extracted for this purpose.

4. RESULTS FOR THE TRAINED CNN MODEL

The CNN output produces a 6-component stress tensor for each depth interval. Shown in Figure 4 is the results for the 1 km depth interval at a single time step. The CNN model results are shown for synthetic examples not used in the model training. The surface displacement from multiple sources varies between ±30 mm. The analytical and CNN predicted stress is shown for each component. With minor exceptions, the CNN well predicts the pattern and location of subsurface stress variation with differences <500 kPa for the example shown. Similar performance and error is observed at all depth intervals.

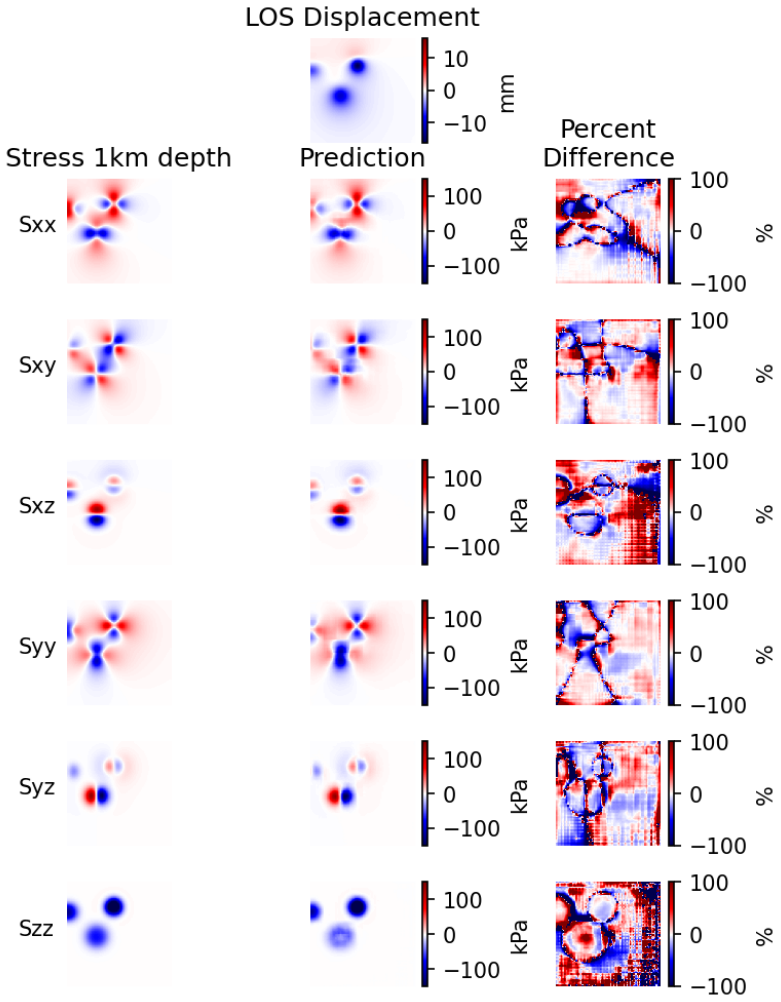

Figure 4: Results for the trained CNN using a synthetic example at a single time step. The single top panel shows the input surface displacement. The left column is the analytical calculated stress, the middle column is the CNN predicted stress, and the right column is the difference.

5. DISCUSSION

A common trade-off with supervised ML applications includes the balance of choosing training data typical to the location of interest and sufficiently robust to construct a trained model to be useful for other locations. A location-specific trained model will reduce the likelihood of achieving spurious solutions at the location of interest, but may also fail to correctly handle unforeseen situations and may be inapplicable to other locations. Conversely, a generally-trained model may be less accurate at any one location. In this work we take a step-wise approach, first establishing the validity of the ML approach for estimating stress changes at the Coso Geothermal field before

applying it to other geothermal fields. With this in mind, we constrain training data to encompass the range of stress sources, both earthquake and injection-related, we expect at Coso. In regard to generalizing the model in the future, it is important to bear in mind that stresses output by the trained CNN are valid only for the set of elastic properties chosen when generating training data. One potential approach to model generalization is to generate a dictionary of trained CNNs, where each entry is trained on a set of elastic properties representative of an endmember environment. We envision only a modest number of trained CNNs would be required to generalize across typical geothermal reservoirs. For instance, three dictionary entries may be sufficient: soft material properties for sedimentary rocks, stiff for crystalline (e.g. the CGF), or layered for sediment overlying crystalline.

Even in light of the Coso-specific training we are employing here, there remains the question of the validity of CNN stresses. We employ analytical models to generate the CNN training data and to benchmark the trained CNN results against variational results. Thus, the key to validating our CNN results depends on the degree to which the analytical models represent actual stress changes at Coso. The key assumptions inherent in the analytical models for earthquake and volumetric sources (Okada, 1992) used here are elastic physics in a half-space. Elastic physics are well established for describing deformation in the shallow crustal depths of the CGF reservoir. We use numerical simulations performed in Abaqus (2019) to determine the degree to which topography and variable material properties at Coso may alter surface deformation due to earthquake or pressure sources. Models are constructed with CGF and regional topography (NASA Shuttle Radar Topography Mission Global 1 Arc Second, 2013) and 3D material properties. We calculate a CGF variable material property model, including Young's Modulus, Poisson's ratio, and density, from smoothed Vp and Vp/Vs tomography models of Zhang and Lin (2014). Four simulations of a cataloged M_w 3.75 earthquake occurring at 3.5 km depth in the CGF were run to determine the impact of topography and 3D material properties, together and separately, on surface deformation (Figure 5). The inclusion of 3D versus uniform material properties account for the only significant variation between model solutions, with 3D material property models producing a maximum difference in vertical surface displacements of ~0.02 mm, or about 7% of the maximum vertical displacement. Comparisons of model solutions with and without topographic variations indicate topography is a negligible factor within a 16 km block around the field. Considering the resolution of InSAR surface displacements are on the order of 1 mm, we deem 3D material properties and topographic effects at the CGF below our observation resolution and that the half-space assumption inherent to our earthquake and pressure analytical models is reasonable. In addition, the minor impact of site-specific material property variation and topography is encouraging evidence that a trained CNN could be transferred to other regions.

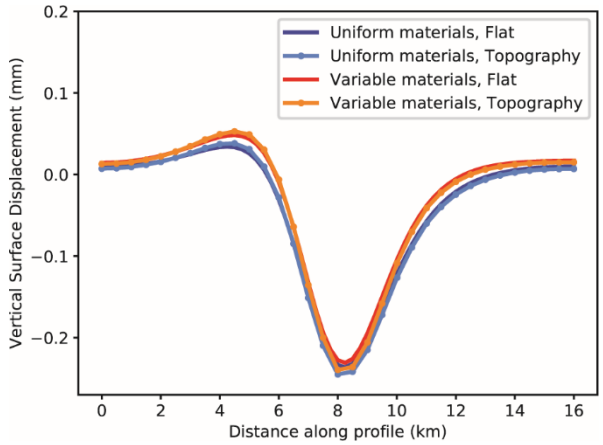

Figure 5: Horizontal profiles of numerically modeled surface displacement from an M_w3.75 earthquake at 3.5 km depth in the CGF. Simulations producing profiles with dotted markers include CGF topographic variations, while smooth profiles do not. Red and orange profile simulations include variable material properties, while dark and light blue profiles include homogeneous, average material properties.

6. CONCLUSIONS

We have developed a novel, CNN-based approach to continuously update a stress model of the Coso Geothermal field. The CNN is trained to translate InSAR surface displacements to a combination of volumetric changes and double couple source mechanisms. Over 10^6 training data scenarios contain deformations due to injection volumes and earthquakes. The injection volume time series contains seasonal and interannual trends. Earthquake sources are randomly located in the horizontal plane, and have magnitudes and depths both characteristic of the field and capable of producing InSAR-measurable surface displacements. The CNN output is a 6-component stress tensor on a two-dimensional grid at depth intervals of 1, 2, 3, and 4 km. The trained CNN well predicts the pattern and location of subsurface stress variation. Future work includes (1) benchmarking the CNN results against variational principle results applied to identical InSAR inputs and (2) undertaking a sensitivity analysis to determine the set of subsurface locations that are well modeled using a single CNN.

ACKNOWLEDGEMENTS

This work was funded with support from the U.S. Department of Energy's Geothermal Technologies Office under the project titled "3.1.8.7 ML: Advanced Characterization of Stress, Critical Stress and Permeability in Geothermal Systems Applying Machine Learning".

REFERENCES

Abaqus, 'Abaqus/CAE 6.11 User's Manual', Dassault Systemes, Providence, RI, USA, (2019).

Ali, S.T., Akerley, J., Baluyut, E.C., Davatzes, N.C., Lopeman, J., and Moore, J.: Geodetic Measurements and Numerical Models of Deformation : Examples from Geothermal Fields in the Western United States, *Proceedings*, 41st Workshop on Geothermal Reservoir Engineering, Stanford University, Stanford, CA, (2016).

Araya-Polo, M., Jennings, J., Adler, A., and Dahlke, T.: Deep-Learning Tomography, *Leading Edge*, **37**, (2018), 58–66.

Bacon, C.R., MacDonald, R., Smith, R.L., and Baedecker, P.A.: Pleistocene High-Silica Rhyolites of the Coso Volcanic Field, Inyo County , California, *Journal of Geophysical Research*, **86**, (1981), 10223–10241.

Bergen, K.J., Johnson, P.A., De Hoop, M. V., and Beroza, G.C.: Machine Learning for Data-Driven Discovery in Solid Earth Geoscience, *Science*, **363**, (2019), 1-10.

Blankenship, D., Blake, K., Calvin, W., DeOreo, S., Faulds, J.E., Glen, J., Hickman, S., Hinz, N., Kaven, O., Lazaro, M., McCulloch, J., Meade, D., Kennedy, M., Phelps, G., Sabin, A., Schoenball, M., Silar, D., Robertson-Tait, A., and Williams, C.: Frontier Observatory for Research in Geothermal Energy: Phase 1 Topical Report West Flank of Coso, CA, (2016).

Buck, C.: Steam Chemistry Monitoring the Navy I Area of the Coso Geothermal Field, *Proceedings*, 45th Workshop on Geothermal Reservoir Engineering, Stanford University, Stanford, CA, (2020).

Cardiff, M., Lim, D.D., Patterson, J.R., Akerley, J., Spielman, P., Lopeman, J., Walsh, P., Singh, A., Foxall, W., Wang, H.F., Lord, N.E., Thurber, C.H., Fratta, D., Mellors, R.J., Davatzes, N.C., and Feigl, K.L.: Geothermal Production and Reduced Seismicity: Correlation and Proposed Mechanism, *Earth and Planetary Science Letters*, **482**, (2018), 470–477.

Christenson, B.W., Kennedy, B.M., Adams, M.C., Bjornstad, S.C., and Buck, C.: Chemical and Isotopic Characteristics of the Coso East Flank Hydrothermal Fluids : Implications for the Location and Nature of the Heat Source, *Proceedings*, 32ndWorkshop on Geothermal Reservoir Engineering Stanford University, Stanford, CA, (2007).

Coso Operating Company – Geothermal Energy Power Plant on China Lake Naval Base, (2020). https://cosoenergy.com/.

Davatzes, N.C., and Hickman, S.H.: Stress and Faulting in the Coso Geothermal Field: Update and Recent Results From the East Flank and Coso Wash, *Proceedings*, 31st Workshop on Geothermal Reservoir Engineering, Stanford University, Stanford, CA, (2006).

Duffield, W.A., Bacon, C.R., and Dalrymple, G.B.: Later Cenozoic Volcanism, Geochronology, and Structure of the Coso Range, Inyo County, California, *Journal of Geophysical Research*, **85**, (1980), 2381–2404.

Eneva, M., Barbour, A., Adams, D., Hsiao, V., Blake, K., Falorni, G., and Locatelli, R.: Satellite Observations of Surface Deformation at the Coso Geothermal Field, California, *Transactions - Geothermal Resources Council*, **42**, (2018), 1383–1401.

Feng, Q., and Lees, J.M.: Microseismicity, Stress, and Fracture in the Coso Geothermal Field, California, *Tectonophysics*, **289**, (1998), 221–238.

Fialko, Y., and Simons, M.: Deformation and Seismicity in the Coso Geothermal Area, Inyo County, California: Observations and Modeling Using Satellite Radar Interferometry, *Journal of Geophysical Research: Solid Earth*, **105**, (2000), 21781–21793.

Geothermal Production and Injection Data Maps, (2020). https://www.conservation.ca.gov/calgem/geothermal/manual/Pages/production.aspx.

Geothermal Well Search, (2020). https://geosteam.conservation.ca.gov/.

Hardebeck, J.L., and Michael, A.J.: Damped Regional-Scale Stress Inversions: Methodology and Examples for Southern California and the Coalinga Aftershock Sequence, *Journal of Geophysical Research: Solid Earth*, **111**, (2006), 1–11.

Hauksson, E., and Unruh, J.: Regional Tectonics of the Coso Geothermal Area along the Intracontinental Plate Boundary in Central Eastern California: Three-Dimensional Vp and Vp/Vs Models, Spatial-Temporal Seismicity Patterns, and Seismogenic Deformation, *Journal of Geophysical Research: Solid Earth*, **112**, (2007), 1–24.

Hauksson, E., Yang, W., and Shearer, P.M.: Waveform Relocated Earthquake Catalog for Southern California (1981 to June 2011), *Bulletin of the Seismological Society of America*, **102**, (2012), 2239–2244.

Jennings, C.W., and Bryant, W.A.: Fault Activity Map of California, (2010).

Lin, J., and Stein, R.S.: Stress Triggering in Thrust and Subduction Earthquakes and Stress Interaction between the Southern San Andreas and Nearby Thrust and Strike-Slip Faults, *Journal of Geophysical Research*, **109**, (2004), 1–19.

Manley, C.R., and Bacon, C.R.: Rhyolite Thermobarometry and the Shallowing of the Magma Reservoir, Coso Volcanic Field, California, *Journal of Petrology*, **41**, (2000), 149–174.

Martínez-Garzón, P., Bohnhoff, M., Kwiatek, G., and Dresen, G.: Stress Tensor Changes Related to Fluid Injection at The Geysers Geothermal Field, California, *Geophysical Research Letters*, **40**, (2013), 2596–2601.

Mhanna, N., Julian, B.R., Foulger, G.R., Sabin, A.E., and Meade, D.: Time-Dependent Seismic Tomography at the Coso Geothermal Area, 1996-2004, *Proceedings*, 43rd Workshop on Geothermal Reservoir Engineering, Stanford University, Stanford, California, (2018).

Monastero, F.C.: Operations at the Coso Geothermal Field in Southern California, *GRC Bulletin*, **September / October** (2002), 188–194.

Monastero, F.C., Katzenstein, A.M., Miller, J.S., Unruh, J.R., Adams, M.C., and Richards-Dinger, K.: The Coso Geothermal Field: A Nascent Metamorphic Core Complex, *Bulletin of the Geological Society of America*, **117**, (2005), 1534–1553.

Moore, J.N., Adams, M.C., Bishop, B.P., and Hirtz, P.: A Fluid Flow Model of the Coso Geothermal System: Data from Production Fluids and Fluid Inclusions, *Proceedings*, 14th Workshop on Geothermal Reservoir Engineering, Stanford University, Stanford, CA, (1989).

Moseley, B., Markham, A., and Nissen-Meyer, T.: Fast Approximate Simulation of Seismic Waves with Deep Learning, *arXiv*, (2018). https://arxiv.org/abs/1807.06873

NASA JPL (2013). NASA Shuttle Radar Topography Mission Global 1 Arc Second. *NASA EOSDIS Land Processes DAAC*. https://doi.org/10.5067/MEaSUREs/SRTM/SRTMGL1.003.

Okada, Y.: Internal Deformation Due to Shear and Tensile Faults in a Half-Space, *Bulletin - Seismological Society of America*, **82**, (1992), 1018–1040.

Reinisch, E.C., Ali, S.T., Cardiff, M., Kaven, J.O., and Feigl, K.L.: Geodetic Measurements and Numerical Models of Deformation at Coso Geothermal Field, California, USA, 2004-2016, *Remote Sensing*, **12**, (2020), 1–23.

Ren, C.X., Hulbert, C., Johnson, P.A., and Rouet-Leduc, B.: Machine learning and fault rupture: a review, *Advances in Geophysics*, **61**, (2020), 57-107.

Rouet-Leduc, B., Jolivet, R., Dalaison, M., Johnson, P.A., and Hulbert, C.: Autonomous Extraction of Millimeter-Scale Deformation in InSAR Time Series Using Deep Learning, *arXiv*, (2020). http://arxiv.org/abs/2012.13849.

Sabin, A., Blake, K., Lazaro, M., Blankenship, D., Kennedy, M., McCullough, J., DeOreo, S., Hickman, S., Glen, J., Kaven, O., Williams, C., Phelps, G., Faulds, J.E., Hinz, N., Calvin, W., Siler, D., and Robertson-Tait, A.: Geologic Setting of the Proposed West Flank Forge Site, California: Suitability for EGS Research and Development, *Transactions - Geothermal Resources Council*, **39**, (2015), 293–301.

Schoenball, M., and Davatzes, N.C.: Quantifying the Heterogeneity of the Tectonic Stress Field Using Borehole Data, *Journal of Geophysical Research: Solid Earth*, **122**, (2017), 6737–6756.

Schoenball, M., Dorbath, L., Gaucher, E., Wellmann, J.F., and Kohl, T.: Change of Stress Regime during Geothermal Reservoir Stimulation, *Geophysical Research Letters*, **41**, (2014), 1163–1170.

Sentinel-1 Observation Scenario, (2021). https://sentinel.esa.int/web/sentinel/missions/sentinel-1/observation-scenario.

Sheridan, J., Kovac, K., Rose, P.E., Barton, C., McCulloch, J., Berard, B., Moore, J.M., Petty, S., and Spielman, P.: In-Situ Stress, Fracture and Fluid Flow Analysis-East Flank of the Coso Geothermal Field, *Proceedings*, 28th Workshop on Geothermal Reservoir Engineering, Stanford University, Stanford, CA, (2003).

Sheridan, J.M., and Hickman, S.H.: In Situ Stress, Fracture, and Fluid Flow Analysis in Well 38C-9: An Enhanced Geothermal System in the Coso Geothermal Field, *Proceedings*, 29th Workshop on Geothermal Reservoir Engineering, Stanford University, Stanford, CA, (2004).

Shoji, D., Noguchi, R., Otsuki, S., and Hino, H.: Classification of Volcanic Ash Particles Using a Convolutional Neural Network and Probability, *Scientific Reports*, **8**, (2018), 1–12.

Spane, F.A.J.: Hydrogeologic Investigation of Coso Hot Springs Inyo County, California, (1978).

Toda, S., Stein, R.S., Sevilgen, V., and Lin, J.: Coulomb 33 Graphic-Rich Deformation & Stress-Change Software for Earthquake, Tectonic and Volcano Research and Teaching - User Guide, USGS Open-File Report 2011-1060, **63**, (2011), https://pubs.usgs.gov/of/2011/1060/of2011-1060.pdf%0Ahttp://pubs.usgs.gov/of/2011/1060/.

Wamalwa, A.M., Mickus, K.L., Serpa, L.F., and Doser, D.I.: A Joint Geophysical Analysis of the Coso Geothermal Field, South-Eastern California, *Physics of the Earth and Planetary Interiors*, **214**, (2013), 25–34.

Wicks, C.W., Thatcher, W., Monastero, F.C., and Hasting, M.A.: Steady State Deformation of the Coso Range, East Central California, Inferred from Satellite Radar Interferometry, *Journal of Geophysical Research*, **106**, (2001), 13769–13780.

Williams, A.E., and Copp, J.F.: Variations in Dissolved Gas Compositions of Reservoir Fluids from the Coso Geothermal Field, *Proceedings*, 16th Workshop on Geothermal Reservoir Engineering, Stanford University, Stanford, CA, (1991).

Wu, Y., and Lin, Y.: InversionNet: An Efficient and Accurate Data-Driven Full Waveform Inversion, *IEEE Transactions on Computational Imaging*, **6**, (2019), 419–433.

Yang, W., Hauksson, E., and Shearer, P.M.: Computing a Large Refined Catalog of Focal Mechanisms for Southern California (1981-2010): Temporal Stability of the Style of Faulting, *Bulletin of the Seismological Society of America*, **102**, (2012), 1179–1194.

Yourgrau, W., and Mandelstam, S.: Variational Principles in Dynamics and Quantum Theory, *Mineola, New York*, **3rd edition**, (1979), 1-224.

Zhang, Q., and Lin, G.: Three-Dimensional Vp and Vp/Vs Models in the Coso Geothermal Area, California: Seismic Characterization of the Magmatic System, *Journal of Geophysical Research: Solid Earth*, **119**, (2014), 4907–4922.